Environmental Chemistry Letters (2020) 18:215–227
https://doi.org/10.1007/s10311-019-00926-5

ORIGINAL PAPER

How to distinguish natural versus engineered nanomaterials: insights from the analysis of TiO_2 and CeO_2 in soils

Zebang Yi[1,2] · Frédéric Loosli[1] · Jingjing Wang[1] · Debora Berti[3] · Mohammed Baalousha[1]

Received: 4 April 2019 / Accepted: 8 August 2019 / Published online: 26 August 2019

Abstract

Increasing amounts of engineered nanomaterials such as TiO_2 and CeO_2 are released into air, waters, soils, and sediments. However, assessing the human-made origin of those nanomaterials is rather difficult because Ti- and Ce-rich particles are naturally present in soils and sediments at concentrations typically much higher than estimated concentrations of engineered nanomaterials. In addition, analysis is complicated by the interactions and aggregation of nanoparticles with environmental particles. Therefore, more knowledge on the properties of natural nanomaterials is needed to distinguish engineered nanomaterials in natural systems. Here, we extracted soil nanomaterials with six extractants and compared recovery and disaggregation to primary particles. Nanomaterials were characterized for hydrodynamic diameter and zeta potential by dynamic light scattering, size-based elemental distribution by field-flow fractionation coupled with inductively coupled plasma-mass spectroscopy, and morphology by transmission electron microscopy. Results show that nanomaterial concentrations increased from CH_3COOH–NaCl–water (lowest), to water or NaCl–water, Na_2CO_3, $Na_4P_2O_7$, and NaCl–$Na_4P_2O_7$ (highest). $Na_4P_2O_7$ was the most efficient extractant that induced the release of primary nanomaterials from microaggregates. Although sodium carbonate extracted relatively high concentrations of nanomaterials, the extracted nanomaterials occurred mainly as aggregates of primary nanomaterials. Ultrapure water, sodium chloride and acetic acid resulted in poor nanomaterial extraction and broad size distributions. Elemental ratios illustrate that Ti is associated with Nb, Ta, and V, and that Ce is associated with rare earth elements such as La, Eu, Y, Ho, Er, Tm, and Yb. Our findings indicate that size, size distribution, and elemental ratios can be used as fingerprints to differentiate engineered nanomaterials such as TiO_2 and CeO_2 from natural nanomaterials in complex media.

Keywords Soil · Natural nanomaterial · Extraction · Characterization · Flow field-flow fractionation · Tetrasodium pyrophosphate

Introduction

The increased production and applications of engineered nanomaterials, such as TiO_2 and CeO_2, result in their release into the environment, where they may pose concerns to living organisms (Piccinno et al. 2012; Dev et al. 2018; Sardoiwala et al. 2018; Lead et al. 2018; Kahlon et al. 2018). Thus, there is a need to develop analytical approaches to quantify the concentrations and characterize the physicochemical properties of engineered nanomaterials in complex environmental matrices including soils and sediments (Alvarez et al. 2009; Rottman et al. 2013). These environmental matrices represent a reservoir for high-concentration natural nanomaterials such as clay particles, Ti, Ce, and Fe oxides, with similar sizes and elemental compositions as engineered nanomaterials (Praetorius et al. 2017; Philippe et al. 2018;

Electronic supplementary material The online version of this article (https://doi.org/10.1007/s10311-019-00926-5) contains supplementary material, which is available to authorized users.

✉ Mohammed Baalousha
mbaalous@mailbox.sc.edu

[1] Department of Environmental Health Sciences, Center for Environmental Nanoscience and Risk, Arnold School of Public Health, University of South Carolina, Columbia, SC 29208, USA

[2] College of Earth Science, Guilin University of Technology, Guilin 541004, China

[3] Virginia Tech National Center for Earth and Environmental Nanotechnology (NanoEarth), 1991 Kraft Dr, Blacksburg, VA 24061, USA

Gondikas et al. 2018). Thus, detection and quantification of engineered nanomaterials in environmental matrices require differentiating engineered from natural nanomaterials (von der Kammer et al. 2012; Montaño et al. 2014). Therefore, a precise knowledge of the properties of natural nanomaterials such as size, size distribution, elemental composition, and elemental ratios is a prerequisite to develop strategies to detect engineered nanomaterials in environmental systems. Nonetheless, characterization of soil natural nanomaterials is challenging because they represent a complex mixture of diverse organic and inorganic particles of different size, chemical composition, structures, etc. (Theng and Yuan 2008; Regelink et al. 2013).

In soils, the majority of inorganic natural nanomaterials form after weathering of parent material. Thus, natural nanomaterials are likely to have similar elemental compositions and associations as those of the forming rocks. For instance, natural TiO_2 minerals, such as rutile and ilmenite, have been shown to be the dominant carrier, e.g., > 90–95% of the whole-rock content, for Ti, Nb, Ta, Sb, and W as well as an important carrier (5–45% of the whole-rock content) for V, Cr, Mo, and Sn in TiO_2-bearing metamorphic rocks (Gaspar and Wyllie 1983; Nakashima and Imaoka 1998). Cerium is the most abundant rare earth element and is typically associated with other rare earth elements such as La, Er, Eu, Ho, Tm, Y, and Yb in minerals such as monazite ($(Ce,La,Th,Nd,Y)PO_4$), xenotime ($(Y,Ce)PO_4$), allanite ($Ca(Ce,La,Y,Ca)Al_2(Fe^{2+},Fe^{3+})(SiO_4)(Si_2O_7)O(OH)$), and bastnasite ($Ca(Ce,La)_2(CO_3)_3F_2$) (Murata et al. 1957; Long et al. 2012). These elemental impurities are generally removed during the manufacturing of TiO_2- and CeO_2-engineered nanomaterials from natural parent minerals resulting in pure TiO_2 and CeO_2 particles (IARC 2010).

Natural nanomaterials in soils tend to associate with organic matter and to form heteroaggregates in the presence of multivalent cations (Buffle et al. 1998). Natural nanomaterials heteroaggregation is one of the key challenges that hamper the characterization and understanding of their physicochemical properties and environmental functions. Various methods have been implemented to extract natural nanomaterials from soils such as physical extraction by filtration, centrifugation, sonication followed by filtration and/or centrifugation, or using chemical extractants such as acetic acid (CH_3COOH), sodium chloride (NaCl), tetrasodium pyrophosphate ($Na_4P_2O_7$), and sodium carbonate (Na_2CO_3) (Siripinyanond et al. 2002; Baalousha et al. 2005; Regelink et al. 2013). Generally, physical extraction approaches result in the extraction of aggregates of natural nanomaterials rather than individual natural nanomaterials, limiting our understanding of the physicochemical proprieties of primary natural nanomaterials. Disaggregation of natural nanomaterial heteroaggregates requires overcoming interaction forces between natural nanomaterials within aggregates such as attractive van der Waals attractions and organo-mineral interactions (Regelink et al. 2013; Loosli et al. 2018) Therefore, using chemical extractants, which can reduce the interaction between natural nanomaterials and soil organic matter (SOM), may disperse higher amount of natural nanomaterials. For example, large amounts of soil organic matter can be extracted using NaOH, Na_2CO_3, and $Na_4P_2O_7$ (Tatzber et al. 2007; van Zomeren and Comans 2007). The latter is also commonly used to disperse soils for particle size fractionation (Pronk and Johnson 1992). Natural nanomaterial extraction from soil microaggregates is a key process to simplify their characterization by reducing natural sample polydispersity and to improve the understanding of natural nanomaterial physicochemical properties such as size distribution, elemental composition and ratios, and morphology.

Asymmetric flow field-flow fractionation is one of the key promising techniques in the nanometrology tool box to detect and quantify engineered nanomaterials, as well as to characterize natural nanomaterials (Baalousha et al. 2005; Meisterjahn et al. 2014). Asymmetric flow field-flow fractionation fractionates nanomaterials according to their diffusion, which can be converted to equivalent hydrodynamic diameter applying Stokes–Einstein equation. When coupled with inductively coupled plasma-mass spectroscopy (ICP-MS), asymmetric flow field-flow fractionation-ICP-MS allows for size fractionation and online analysis of nanomaterial elemental composition. A critical step in asymmetric flow field-flow fractionation analyses of soil natural nanomaterials is the suspension of the primary natural nanomaterials into colloidally stable suspension.

This study aims to (1) evaluate the efficiency of six different extractants to disperse natural nanomaterials from soil and (2) characterize physicochemical properties of the extracted natural nanomaterials such as size distribution, morphology, elemental composition, and ratios by ICP-MS, asymmetric flow field-flow fractionation-ICP-MS, and transmission electron microscope (TEM).

Materials and methods

Site description and sampling

A topsoil sample used in this study was sampled in Dillon County (34.505355°N, 79.424219°W) which is situated in the coastal plain region of South Carolina, USA. The soil was characterized as Lucy series (taxonomic class: loamy, kaolinitic, thermic Arenic Kendiudults) which consists of very deep, well-drained, moderately permeable soils on uplands (NCSS 2019). These series formed in sandy, loamy marine, and fluvial sediments of the southern coastal plain in the USA. The soil sample was collected from the A horizon

which consists mainly of loamy fine sand (NCSS 2019). The soil sample is characterized by dark grayish brown color, with weak fine granular structure. The sampling site was chosen in a natural reserve to avoid possible anthropogenic nanomaterial contamination. The soil was sampled using a hand drill and was preserved in a polyethylene bag. All samples were air-dried and sieved through a 2-mm nylon sieve (Zhangxing Brand, Zhangxing Instrument, China) to remove gravel and large organic debris.

Soil extraction protocols

Natural nanomaterials were extracted from the soil using six different extraction protocols: (1) ultrapure water (PURELAB Option-Q, ELGA LabWater, UK) (Tang et al. 2009), (2) prewashing in 0.1 M sodium chloride (NaCl, VWR Analytical, BDH®, ACS, USA) to exchange divalent cations followed by extraction in ultrapure water (Plathe et al. 2010; Navratilova et al. 2015), (3) prewashing in 1 M acetic acid (CH_3COOH, BDH Chemicals, ACS grade, USA) to remove carbonates, followed by a second prewashing in 0.1 M NaCl, followed by extraction in ultrapure water (Baalousha et al. 2006), (4) 2 mM tetrasodium pyrophosphate ($Na_4P_2O_7$, Alfa Aesar, Analytical grade, Japan) (Regelink et al. 2013), (5) prewashing in 0.1 M NaCl followed by extraction in 2 mM $Na_4P_2O_7$, and (6) 0.1 M sodium carbonate (Na_2CO_3) (Li et al. 2012).

For the prewashing step/steps, 40 mL of NaCl or CH_3COOH was added to 4 g of soil in 50 mL polypropylene centrifuge tubes (Eppendorf, Mexico). The suspensions were overhead shaken with a tube rotator (Fisher Scientific, China) at 40 rpm overnight. The suspensions were then centrifuged at 10,000×*g* for 4 h, a sufficient force to sediment all soil aggregates larger than 40 nm with a density of 2.5 g cm^{-3}. Thirty-five milliliters of supernatant was removed carefully with a manual pipette to avoid resuspension of the soil and 35 mL of next-step chemical extractant was added. The suspension was again shaken overnight. For the protocols without prewashing step, the same mass of soil and ratio was used as well as the overnight soil wetting under overhead shaking. The soil suspensions were then sonicated for 1 h in an ultrasonication bath (Branson, Model 2800, 40 kHz, USA) to disrupt soil microaggregates and release natural nanomaterials. Natural nanomaterials were then isolated from larger particles by centrifugation at 3100×*g* for 130 min to obtain a 100-nm size cut-off based on a particle density of 2.5 g cm^{-3} and Stokes' law (Tang et al. 2009). Centrifugation rather than filtration was applied to separate natural nanomaterials from larger particles as centrifugation results in lower particle losses compared to filtration (Fedotov et al. 2011). The top 25 mL of supernatant was collected and stored in the dark at 4 °C until further analysis. All polymer containers/tubes were acid cleaned with 5% HNO_3 (Sigma-Aldrich, ACS, USA) for 24 h and then thoroughly rinsed three times with ultrapure water.

General properties of soil natural nanomaterials extracts

The pH of the extracted natural nanomaterial suspensions was measured immediately after extraction using a pH meter (Mettler Toledo, FiveEasy, Switzerland). The dissolved organic matter concentration in the extracted natural nanomaterial suspensions was measured using a total organic carbon (TOC) analyzer (Shimadzu TOC-l CSN E-100, Japan). The z-average hydrodynamic diameter and zeta potential of the extracted natural nanomaterial suspensions were determined by dynamic light scattering (DLS) and laser Doppler electrophoresis techniques, respectively (Malvern, Nano-ZS, USA). The Smoluchowski approximation was used for zeta-potential determination (Baalousha et al. 2012).

Elemental analysis of the extracted soil natural nanomaterials

The extracted natural nanomaterial suspensions were digested in 15 mL Teflon vessels (Savillex, USA) on custom-made Teflon-covered hot plates with double-high-efficiency particulate air (HEPA)-filtered forced air in a metal-free HEPA-filtered air clean laboratory. All vessels were thoroughly cleaned using aqua regia. The HNO_3 + HF, double-distilled with Teflon homemade boiler, digestion method was performed according to the procedure described elsewhere (Frisby et al. 2016; Loosli et al. 2019). Aliquots of natural nanomaterial suspensions (5 mL) were weighted into a Teflon vessel and dried on custom-made Teflon-covered hot plates at 110 °C. The dried samples were treated with approximately 1 mL H_2O_2 to remove organic matter and were kept on the hot plate until complete dryness. A mixture of HF/HNO_3 at 3:1 ratio was slowly added to the H_2O_2-treated samples. The vessels were then sealed and placed on the hot plate preset at 110 °C overnight. The vessels were then uncapped, and the samples were dried again slowly at 80 °C to minimize the formation of insoluble fluorides. Once dry, the samples were dissolved in 1 mL distilled HNO_3 and dried again on a hot plate preset at 110 °C, and this procedure was repeated two times. The samples were dissolved in 10 mL 1% HNO_3, and the vessels were sealed and heated in an oven at 50 °C until the materials in the vessels dissolved fully. Then, the resulting solutions were transferred into acid-washed centrifuge tubes and preserved at 4 °C in the dark until further analysis. Samples were centrifuged at 3100×*g* for 5 min prior analysis to remove any undigested refractory materials.

Elemental concentrations of the digested natural nanomaterial suspensions were performed on an ELEMENT 2 high-resolution-inductively coupled plasma-mass spectroscopy (HR-ICP-MS) following the established protocols (Frisby et al. 2016). Samples were injected to the ICP-MS using an APEXQ introduction system and a 100 µl min^{-1} perfluoroalkoxy alkanes (PFA) nebulizer (~ 120–150 µL min^{-1} actual uptake). Amplifier gain calibration was performed daily. Baseline was determined by beam deflection. Typical runs consisted of 35–40 integrations (8.3 s). The analytes chosen were ^{27}Al, ^{45}Sc, ^{47}Ti, ^{51}V, ^{55}Mn, ^{57}Fe, ^{59}Co, ^{63}Cu, ^{93}Nb, ^{107}Ag, ^{115}In, ^{139}La, ^{140}Ce, ^{144}Nd, ^{153}Eu, ^{159}Tb, ^{165}Ho, ^{166}Er, ^{169}Tm, ^{174}Yb, ^{175}Lu, ^{178}Hf, and ^{208}Pb. Elements with potential interferences, e.g., Al, Ca, Co, Cr, Cu, Fe, Ga, Mg, Mn, Ni, Ti, V, and Zn, were measured in medium resolution, e.g., $m/\Delta m = 4000$, while the rest in low resolution for maximum sensitivity ($m/\Delta m = 300$). Concentrations were calculated against a multi-element standard solution composed of a mixture of IV-ICP-MS-71A (ICP-MS Complete Standard, Inorganic Ventures, USA) and ICP-MS-68A-B (68 Element Standard, High-Purity Standards, USA) multi-element standards.

The elemental concentrations of the U.S. Geological Survey (USGS) reference materials BCR-2 and BIR-1 basalts run as unknowns after digestion following the digestion procedure described above demonstrated high recovery, e.g., approximately 100%, for most elements (Loosli et al. 2019). The digestion and analysis methods precision were 2–3% and accuracy was better than 5% for most elements, including Ti, Ce, and Nb and rare earth elements. Full procedural digestion blanks were < 4% of samples' analyte signal. Therefore, blanks are insignificant to the calculations of elemental concentrations or total elemental ratios (Loosli et al. 2019).

Size-based elemental analysis

Nanomaterial size-based elemental distribution was measured by asymmetric flow field-flow fractionation (Wyatt Eclipse® DualTec™ AF4, USA) coupled online with ICP-MS (PerkinElmer NexION350D, USA). The asymmetric flow field-flow fractionation was equipped with 350 µm spacer and a 1-kDa polyether sulfonate membrane (PES, Palls Corporation, USA). The asymmetric flow field-flow fractionation carrier solution consisted of 10 mM $NaNO_3$ (ACS grade, AMRESCO, USA) at pH 10. The cross flow and the detector flow were set to 1.0 mL min^{-1}. Latex nanosphere standards of 20, 40, 80, and 150 nm (Thermo Scientific, USA) were used to calibrate particle size versus elution time. Sample injection volume was 20 µL for all samples with 10-min focus time. $Na_4P_2O_7$-extracted natural nanomaterials were analyzed again by asymmetric flow field-flow fractionation-ICP-MS with an injection volume of 100 µL for better detection and quantification of trace elements such as Nb and Ta. All samples were sonicated in a bath sonicator for 10 min prior injection into the asymmetric flow field-flow fractionation to disperse any loosely aggregated natural nanomaterials.

The ICP-MS was calibrated for the concentration range of 0.1–100 µgL^{-1} using a mixture of two multi-element standards IV-ICP-MS-71A) and ICP-MS-68A-B (68 Element Standard, High-Purity Standards, USA). Multi-element internal standard including ^{6}Li, ^{45}Sc, ^{89}Y, ^{115}In, ^{159}Tb, and ^{209}Bi, at a concentration of 10 µg L^{-1} (ICP Internal Element Group Calibration Standard, BDH Chemicals, USA) was continuously introduced following natural nanomaterial separation by asymmetric flow field-flow fractionation and prior ICP-MS analyses via a Y-connector (Analytical Sales & Services Inc., USA) to monitor any potential signal drift overtime. A 20-min 1% HNO_3 rinse and a 10-min ultrapure water rinse were applied between consecutive samples to clean the tubing. Data were collected using Chromera 4.1.0.6386 software. Asymmetric flow field-flow fractionation-ICP-MS fractograms were smoothed in OriginPro 8 software using the Savitzky–Golay convolution method (Luo et al. 2005). Elemental recovery in the asymmetric flow field-flow fractionation channel was calculated as the total area of the fractograms divided by the total elemental mass in the injected volume according to Eq 1.

$$\text{Elemental recovery} = \frac{\text{Total area of the fractogram}}{\text{VC}} \times 100\% \quad (1)$$

where V is the injection volume and C is the elemental concentration in the injected sample.

Transmission electron microscopy

Natural nanomaterials morphological and elemental analysis of selected soil natural nanomaterial suspensions extracted using NaCl–ultrapure water, CH_3COOH–NaCl–ultrapure water, NaCl–$Na_4P_2O_7$, and Na_2CO_3 were performed independently at the National Center for Earth and Environmental Nanotechnology (NanoEarth) at Virginia Tech using Jeol 2100 Transmission Electron Microscope (TEM) operated at 200 keV and equipped with a LaB_6 filament and a Jeol EX-230 Silicon Drift Detector (SDD) with a 60-mm^2 window of acquisition for energy-dispersive spectroscopy. Micrographs were acquired at different magnifications, ranging from 500× to 400,000×, to gather information about the average size, morphology, and degree of aggregation of nanomaterials on the grid. TEM data were used qualitatively to underpin other analytical techniques as approximately 20 particles were imaged for each sample, which were not sufficient to determine the particle size distribution of the extracted natural nanomaterials.

TEM samples were prepared using drop deposition method according to the procedure described elsewhere (Baalousha et al. 2014; Prasad et al. 2015). Briefly, TEM grids were functionalized using a positively charged poly-L-lysine (1% w/v in water solution; Ted Pella, USA) to enhance the attachment of the negatively charged natural nanomaterials on the grid surface. Ten microliters poly-L-lysine was deposited on a 300-mesh Cu grid (Ted Pella, Pelco®, USA) for 20 min followed by rinsing three consecutive times in ultrapure water to remove excess poly-L-lysine. Subsequently, 20 µL of soil natural nanomaterial suspensions was deposited on the poly-L-lysine functionalized TEM grids for 15 min. The excess natural nanomaterial suspension was then removed by immersing the TEM grid three times in ultrapure water to avoid natural nanomaterial aggregation during the drying process. The TEM grids were then left to dry (12 h) in a covered petri dish to avoid atmospheric particle deposition on the TEM grid.

Results and discussion

Effect of extractants on properties of natural nanomaterial suspensions

The physicochemical properties of the extracted natural nanomaterial suspensions obtained using six different extractants including pH, dissolved organic carbon (DOC), z-average hydrodynamic diameter, zeta potential, and total metal concentration are summarized in Tables S1 and 2 and Fig. S1. The extracted natural nanomaterial suspension pH varied from 4.3 to 10.9, with the lowest pH measured in the CH_3COOH–NaCl–Ultrapure water-extracted natural nanomaterial suspension and the highest pH measured in the Na_2CO_3-extracted natural nanomaterial suspension (Table S1). The DOC concentration varied from 350 to 2870 mg kg^{-1}, with lowest DOC (< 350 mg kg^{-1}) concentration for CH_3COOH–NaCl–ultrapure water-extracted natural nanomaterial suspension and highest (> 2800 mg kg^{-1}) DOC concentration for (NaCl–$Na_4P_2O_7$)- and Na_2CO_3-extracted natural nanomaterial suspensions. In general, DOC concentration in the extracted natural nanomaterial suspensions increased with the increase in pH (Fig. S1a). However, the concentration of DOC in (NaCl–$Na_4P_2O_7$)-extracted natural nanomaterial suspension is similar to that in Na_2CO_3-extracted natural nanomaterial suspension despite the lower pH of $Na_4P_2O_7$-extracted natural nanomaterial suspension, indicating that $Na_4P_2O_7$ is more efficient in extracting DOC than Na_2CO_3 and thus in breaking soil microaggregates. The lowest DOC concentration measured in the CH_3COOH-extracted natural nanomaterial suspensions can be attributed to the low pH, ca. 4.3, which may prevent DOC desorption from organo-mineral surfaces (Illés and Tombácz 2006) and thus prevent soil aggregate breakup. The zeta potential varied from − 20.4 to − 38.0 mV. As a rule of thumb, particles having the zeta potential higher than +30 mV or lower than − 30 mV are considered as stable suspensions (Tunç et al. 2012). Thus, the magnitude of the zeta potential indicates the stability of the extracted natural nanomaterials. The magnitude of zeta potential increased following the order of ultrapure water < Na_2CO_3 < CH_3COOH–ultrapure water < NaCl–ultrapure water ~ $Na_4P_2O_7$ < NaCl–$Na_4P_2O_7$. The z-average hydrodynamic diameter of natural nanomaterial suspensions decreased from 99 ± 7 to 82 ± 3 nm, following the order: ultrapure water ~ CH_3COOH–NaCl–ultrapure water ~ Na_2CO_3 > NaCl–ultrapure water > $Na_4P_2O_7$ > NaCl–$Na_4P_2O_7$ (Table S1). The z-average hydrodynamic diameter decreased with the increase in zeta-potential magnitude (Fig. S1b). This is because the higher zeta-potential magnitude results in higher electrostatic repulsion forces between natural nanomaterials within aggregates, and thus increase natural nanomaterial aggregate breakup (Baalousha 2009).

Effect of extractants on elemental concentrations of natural nanomaterial suspensions

Total elemental concentrations in the extracted natural nanomaterial suspensions increased following the order CH_3COOH–NaCl–ultrapure water < ultrapure water ≈ NaCl–ultrapure water < Na_2CO_3 < $Na_4P_2O_7$ < NaCl–$Na_4P_2O_7$ (Fig. 1, Fig. S2, and Table S2). Compared to ultrapure water or NaCl–ultrapure water extractions, the total elemental concentrations were twofold to 5.5-fold higher in (NaCl–$Na_4P_2O_7$)-extracted natural nanomaterial suspension, 2.1–4.5-fold higher in $Na_4P_2O_7$-extracted natural nanomaterial suspension, 1.5–4.8-fold higher in Na_2CO_3-extracted natural nanomaterial suspension, and twofold to tenfold lower for CH_3COOH–NaCl–ultrapure water-extracted natural nanomaterials (Fig. S2). Thus, $Na_4P_2O_7$ and Na_2CO_3 are the most efficient extractants to disperse natural nanomaterial from soil, whereas CH_3COOH–NaCl–ultrapure water is the less efficient to disperse natural nanomaterials from soils. In general, the total elemental concentrations in the extracted natural nanomaterial suspensions increased with the increase in pH and DOC concentration (Figs. S3 and S4). Metal concentrations in $Na_4P_2O_7$-extracted natural nanomaterial suspensions were above the pH-metal concentration correlation line due to the higher extraction of natural nanomaterials (Fig. S3). The normalized total elemental concentrations, i.e., $[M_{protocol}]/[M_{Ultrapure\ water}]$, were relatively constant for all elements in the case of (NaCl–ultrapure water)- and CH_3COOH–NaCl–ultrapure water-extracted natural nanomaterials, suggesting no preferential/selective extraction of natural nanomaterials using these methods (Fig. S2). On the other hand, $[M_{NaCl–Na4P2O7}]/[M_{Ultrapure\ water}]$

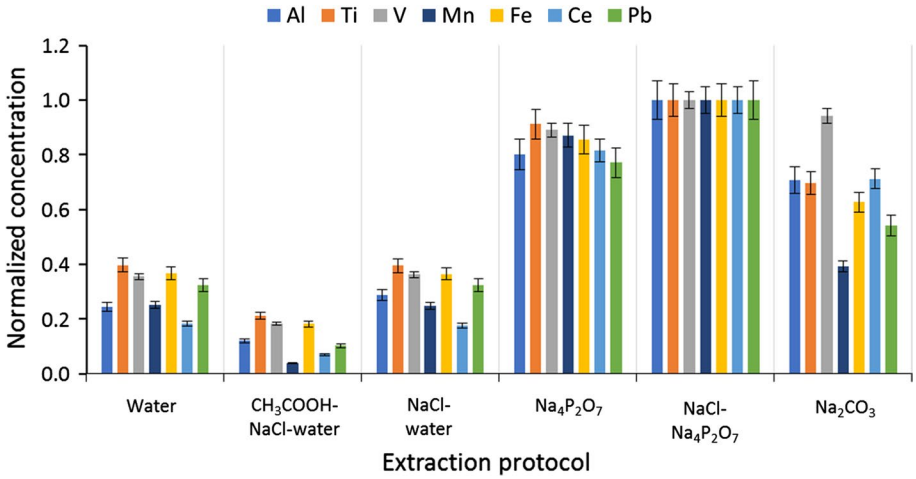

Fig. 1 Normalized metal concentrations in the extracted natural nanomaterial suspension as a function of extraction protocols. Metal concentration was normalized to the highest concentrations measured among all extraction protocols, i.e., NaCl–$Na_4P_2O_7$ extraction. The total elemental concentrations in the extracted natural nanomaterial suspensions were twofold to 5.5-fold higher in NaCl–$Na_4P_2O_7$-extracted natural nanomaterial suspension and 2.1–4.5-fold higher in $Na_4P_2O_7$-extracted natural nanomaterial suspension compared to ultrapure water (water) or NaCl–ultrapure-extracted natural nanomaterial suspensions

varied from 2.3 for Ta to 5.5 for Ce, suggesting the preferential/selective extraction of Ce-rich natural nanomaterials compared to Ti-rich natural nanomaterials. A similar trend but with lower $[M_{Na2CO3}]/[M_{Ultrapure\ water}]$ was observed for Na_2CO_3-extracted natural nanomaterials.

The amount of dispersed natural nanomaterials increased following the order CH_3COOH–NaCl–ultrapure water < ultrapure water ~ NaCl–ultrapure water < Na_2CO_3 < $Na_4P_2O_7$ < NaCl–$Na_4P_2O_7$. The differences in the extraction efficiency between these six extractants can be attributed to the differences in their capacity to disperse and stabilize natural nanomaterials. Ultrapure water, CH_3COOH, and NaCl are mild extractants which can be used to mimic the soil pore water (Koopmans and Groenenberg 2011) and to disperse the potentially mobile soil natural nanomaterials (Kretzschmar and Sticher 1997). Apparently, the zeta potential of the natural nanomaterials is not sufficiently negative to overcome organo-mineral interactions and/or the van der Waals interactions between natural nanomaterials and thus is not sufficient to cause suspension of natural nanomaterials under these conditions. NaCl is widely used for cation exchange to displace multivalent cations in soil microaggregates (Baalousha et al. 2005; Navratilova et al. 2015). NaCl–ultrapure water results in a slight increase in DOC concentration (Table S1) and small differences in natural nanomaterial size distribution compared to ultrapure water-extracted natural nanomaterials (Fig. 2 and Fig. S5). The cation exchange using NaCl results in partial disaggregation of natural nanomaterial aggregates but does not result in a significant increase in the concentration of the extracted natural nanomaterials compared to ultrapure water (Fig. 1). This is likely because NaCl is not sufficient to break the organo-mineral bonds (evident by the slight increase in DOC concentration, Table S1).

The dispersion of natural nanomaterials in $Na_4P_2O_7$ coincides with the extraction of a large fraction of soil organic matter (SOM). Compared to ultrapure water, CH_3COOH–NaCl–ultrapure water, and NaCl–ultrapure water, $Na_4P_2O_7$ extracted more natural nanomaterials and more SOM. This is in agreement with previous studies that demonstrated that the removal of SOM enhances the suspension of nanomaterials from soil (Calabi-Floody et al. 2011). The suspension capacity of $Na_4P_2O_7$ can be explained by two factors (Pansu and Gautheyrou 2007). First, pyrophosphate, being a tetravalent anion, is a very effective competitor for SOM adsorbed on natural nanomaterial surfaces (Regelink et al. 2013). The replacement of SOM by pyrophosphate leads to a more negative zeta potential of the natural nanomaterials, which induce suspension of these natural nanomaterials. Second, pyrophosphate acts as a ligand for di- and trivalent cations such as Ca^{2+}, Al^{3+}, and Fe^{3+}. The complexation of these metals by pyrophosphate during soil extraction reduces the concentration of free multivalent cations, i.e., counterions for negatively charged particles, and thus reduces the aggregation between natural nanomaterials and/or between natural nanomaterials and SOM and increase natural nanomaterial surface charge and their dispersion. Natural organic matter (NOM) adsorbs on natural nanomaterial surfaces, forms a surface coating, and stabilizes natural nanomaterials. Multivalent cations such as Ca^{2+}, Mg^{2+}, Fe^{3+}, and Al^{3+} destabilize NOM-coated natural nanomaterials via bridging mechanism, resulting in the formation of large aggregates (Chen et al. 2006). The sequestration of multivalent cations by pyrophosphate will

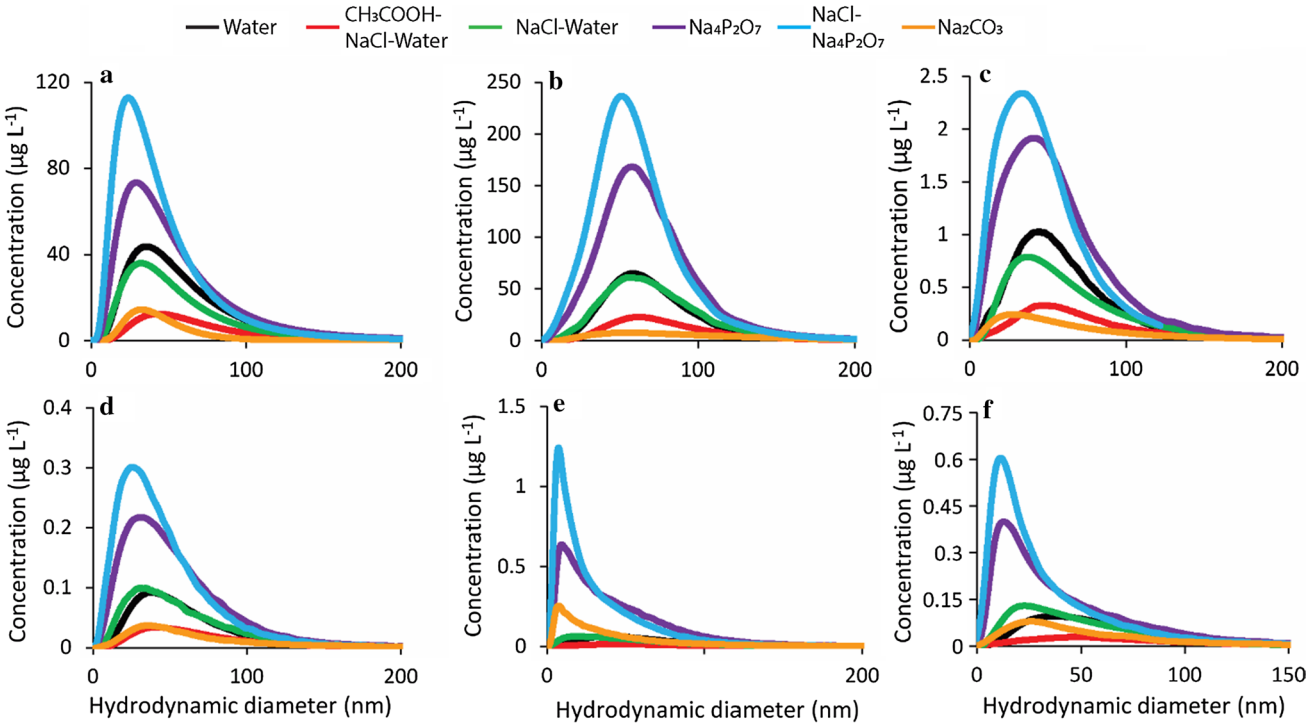

Fig. 2 Size distribution of natural nanomaterials measured by asymmetric flow field-flow fractionation coupled with inductively coupled plasma-mass spectrometer for **a** Fe, **b** Al, **c** Ti, **d** V, **e** Ce, **f** Mn. Natural nanomaterial size distributions generally shift toward smaller sizes following the order CH_3COOH–NaCl–ultrapure water > ultrapure water > NaCl–ultrapure water > Na_2CO_3 > $Na_4P_2O_7$ > NaCl–$Na_4P_2O_7$. Elemental concentration increase with extractant concentration. The different extractants have a slight effect on the size distribution of Fe, Al, Ti, and V, whereas they have a more pronounced influence on the size distribution of Ce and Mn. Injection volume was 20 µl

thus reduce SOM-coated natural nanomaterial bridging and enhance natural nanomaterial suspension. Carbonate has less affinity to di- and trivalent cations, e.g., solubility product of $CaCO_3 = 3.36 \times 10^{-9}$ M^2, than phosphate, e.g., solubility product of $Ca_3(PO_4)_2 = 2.53 \times 10^{-33}$ M^5, resulting in relatively higher free cations during soil extraction, and thus leads to more aggregation of SOM and natural nanomaterials and decreased natural nanomaterial suspension compared to pyrophosphate. According to Schulze–Hardy rule, the destabilizing power of a counter ion is proportional to its valency (Verrall et al. 1999). Thus, multivalent counter ions are more efficient than monovalent counterions in screening natural nanomaterial surface charge and inducing their aggregation.

Effect of extractants on natural nanomaterial size distribution

Element-specific natural nanomaterial particle size distribution measured by asymmetric flow field-flow fractionation inductively coupled plasma-mass spectroscopy (asymmetric flow field-flow fractionation-ICP-MS) as a function of the used extractant is presented in Fig. 2 for selected elements representing the major natural nanomaterial phases in soils including Fe, Al, Ti, V, Ce, and Mn. The peak-normalized size distributions (Fig. S5) demonstrate that natural nanomaterial size distributions generally shift toward smaller sizes following the order CH_3COOH–NaCl–ultrapure water > ultrapure water > NaCl–ultrapure water > Na_2CO_3 > $Na_4P_2O_7$ > NaCl–$Na_4P_2O_7$. The extractants have only a slight effect on the size distribution of Fe, Al, Ti, and V (Fig. 2a–d), whereas they have a more pronounced influence on the size distribution of Ce and Mn (Fig. 2e and f and Fig. S5). For instance, Ti and Fe modal size shifted slightly from 50 nm for CH_3COOH–NaCl–ultrapure water-extracted natural nanomaterials to 30–35 nm for NaCl–$Na_4P_2O_7$-extracted natural nanomaterials, whereas Ce and Mn modal size shifted more substantially from ca. 50 nm for CH_3COOH–NaCl–ultrapure water-extracted natural nanomaterials to 5–8 nm for NaCl–$Na_4P_2O_7$-extracted natural nanomaterials, indicating the higher extent of small Ce- and Mn-containing natural nanomaterials for $Na_4P_2O_7$-extracted natural nanomaterials. This is in agreement with the significantly highly selective extraction of Ce and Mn particles by $Na_4P_2O_7$ (Fig. 1 and Fig. S2). The majority (67.3–79.4%) of Ce in $Na_4P_2O_7$- and NaCl–$Na_4P_2O_7$-extracted natural nanomaterials occur in

the size range 0–50 nm. This is likely due to partial release of Ce-containing primary natural nanomaterials with size in the range 0–50 nm. Ce-containing natural nanomaterials > 50 nm are likely to be associated with other natural nanomaterial phases such as Ti- and Fe-rich natural nanomaterials.

Elemental concentrations generally increase following the order CH_3COOH–NaCl–ultrapure water < ultrapure water ~ NaCl–ultrapure water < Na_2CO_3 < $Na_4P_2O_7$ < NaCl–$Na_4P_2O_7$. This trend agrees with the total metal concentration measured in natural nanomaterial suspensions (Fig. 1), except for Na_2CO_3-extracted natural nanomaterials. The lower elemental concentration for Na_2CO_3-extracted natural nanomaterials could be attributed to the broader natural nanomaterial particle size distribution, or the loss of natural nanomaterials in the asymmetric flow field-flow fractionation channel. These hypotheses are supported by the natural nanomaterial elution at the end of the asymmetric flow field-flow fractionation run, when the cross flow is reduced to 0 mL min^{-1}, indicating the retention of natural nanomaterials in the channel. The % elemental concentrations obtained by asymmetric flow field-flow fractionation-ICP-MS relative to the total elemental concentration measured by ICP-MS following total digestion is generally > 60% (varies in the range 50–141.9%) for ultrapure water-, NaCl–ultrapure water-, $Na_4P_2O_7$-, and NaCl–$Na_4P_2O_7$-extracted natural nanomaterials (Table S3), suggesting that the large majority of the metals were extracted in the form of natural nanomaterials. The low recovery of natural nanomaterials for (CH_3COOH–NaCl–ultrapure water)- and Na_2CO_3-extracted natural nanomaterials is likely due to the extraction of aggregated natural nanomaterials and the interaction with the asymmetric flow field-flow fractionation membrane during the separation process.

Figure S5 presents natural nanomaterial particle size distribution for peak-normalized element concentration of Fe, Al, Ti, V, Ce, and Mn as a function of the extraction protocols. The elemental size distributions of natural nanomaterials extracted using ultrapure water (Fig. S5a) and NaCl–ultrapure water (Fig. S5b) are overlaid on top of each other (except for Al) and show a relatively broad size distribution, e.g., 0–200 nm, indicating that the extracted natural nanomaterials are formed of small aggregates of primary natural nanomaterials and thus that these extraction protocols are insufficient to break such aggregates into primary natural nanomaterials. The larger size measured by asymmetric flow field-flow fractionation-ICP-MS compared to the theoretical centrifugation size cut-off, e.g., 100 nm, can be attributed to the: (1) lower density of the extracted natural nanomaterials than the assumed natural nanomaterial density of 2.5, which will result in the retention of larger natural nanomaterials in the supernatant, and (2) deviation of particle shape, e.g., clays platelets, from the spherical particles used for asymmetric flow field-flow fractionation calibration. CH_3COOH–NaCl–ultrapure water-extracted natural nanomaterials (Fig. S5c) size distribution for Al did not change in comparison with ultrapure water-extracted natural nanomaterials. The early elution of Fe, Ti, V, Ce, and Mn indicates the potential of CH_3COOH–NaCl–ultrapure water extraction to break some natural microaggregates, resulting in release of small natural nanomaterial aggregates and/or primary particles, although the extraction efficiency is low (Fig. 2). The elemental size distributions of natural nanomaterials extracted using $Na_4P_2O_7$ (Fig. S5d) and NaCl–$Na_4P_2O_7$ (Fig. S5e) show narrower size distribution range (ca. 0–150 nm) compared to those extracted by ultrapure water and follow the order Al > Ti > V ~ Fe > Mn > Ce. These results suggest that $Na_4P_2O_7$ results in disaggregation and release of mainly primary natural nanomaterials from soil microaggregates. The elemental size distributions of Na_2CO_3-extracted natural nanomaterials (Fig. S5f) show narrow size distribution for Ce, broad size distribution for Al, and intermediate size distribution for Ti, Fe, V and Mn. The elemental size distributions of Na_2CO_3-extracted natural nanomaterials also show a broader size distribution for all elements compared to $Na_4P_2O_7$- and NaCl–$Na_4P_2O_7$-extracted natural nanomaterials (Fig. S5d and e). These results together with the lower elemental recovery for Na_2CO_3-extracted natural nanomaterials (Table S3) indicate that Na_2CO_3 extracts natural nanomaterials in the form of aggregates. These findings were further corroborated by transmission electron microscope (TEM) analysis (Fig. S6). TEM micrographs illustrate that natural nanomaterials extracted by different extraction protocols are characterized by different morphologies and sizes. NaCl–ultrapure water- and CH_3COOH–NaCl–ultrapure water-extracted natural nanomaterials occur as aggregates of natural nanomaterials (Fig. S6a and b), whereas $Na_4P_2O_7$- and Na_2CO_3-extracted natural nanomaterials occur mainly as single particles (Fig. S6c and d). Energy-dispersive spectroscopy analysis (data not presented) demonstrates that the majority of detected natural nanomaterials contained Al and Fe in good agreement with the high concentrations of Al and Fe measured by total digestion (Table S2) and asymmetric flow field-flow fractionation-ICP-MS (Table S3).

Elemental association and ratios

Natural nanomaterials contain a mix of elements which can be used to distinguish them from anthropogenic and/or engineered nanomaterials (Gondikas et al. 2014). Thus, this section discusses the natural association between elements as a fingerprint for natural nanomaterials and the impact of extraction protocols on elemental associations. Below we discuss elemental ratios obtained by total digestion for natural nanomaterials extracted using different protocols and

size-dependent elemental ratios determined by asymmetric flow field-flow fractionation-ICP-MS for (NaCl–$Na_4P_2O_7$)-extracted natural nanomaterials.

The elemental ratio of Zr to Hf was constant, e.g., ~ 27.8 ± 0.9, for all extraction protocols (Fig. S7), indicating the strong association between Zr and Hf in the extracted natural nanomaterials. Zirconium and hafnium are refractory lithophile elements that have nearly identical arrangement of the outmost electron, charge, atomic and ionic radii, e.g., atomic radius: Zr = 1.45 Å, Hf = 1.44 Å; ionic radius: Zr^{4+} = 0.74 Å, Hf^{4+} = 0.75 Å, and ionic potentials (Wedepohl 1969). Thus, they and other similar elements, such as niobium, thorium, and uranium, develop intense electrostatic fields and do not substitute for the major elements in ordinary minerals (Jones et al. 2017). Instead, these elements concentrate in less common accessory minerals. Zircon ($ZrSiO_4$) is the most common natural occurring zirconium- and hafnium-bearing mineral. Although zircon is only an accessory mineral in igneous and sedimentary rocks, it incorporates ~ 1 wt% of Hf into its crystal structure and controls the bulk rock Hf budget of most crustal rocks (Patchett et al. 1982). This leads to a very strong correlation, i.e., 0.97 and 0.96, between Zr and Hf in subsoils and in topsoils (Patchett et al. 1982). Most natural zircon has a Zr/Hf ratio of 33.6 to 1, which is about the same as the average crustal abundance ratio of those elements (Taylor and McLennan 1985). Hf is incorporated into the crystal structure of zircon by isomorphism, and a similar process will occur during chemical treatment (Abbaspour and Baramakeh 2006; Morel et al. 2008); thus, the Zr/Hf ratio is maintained during the digestion process.

The elemental ratios of Ce to rare earth elements (Fig. 3a and b) calculated based on total elemental concentrations were constant for natural nanomaterials extracted using different extractants, except for carbonate-extracted natural nanomaterials which show higher elemental ratios compared to the other extraction protocols (Fig. 3a and b). The elemental ratio of Ce to La, Er, Yb, Eu, Ho, and Tm shows relatively constant ratios throughout the size range 20–100 nm, with a small increase for particles < 20 nm (Fig. 3c) due

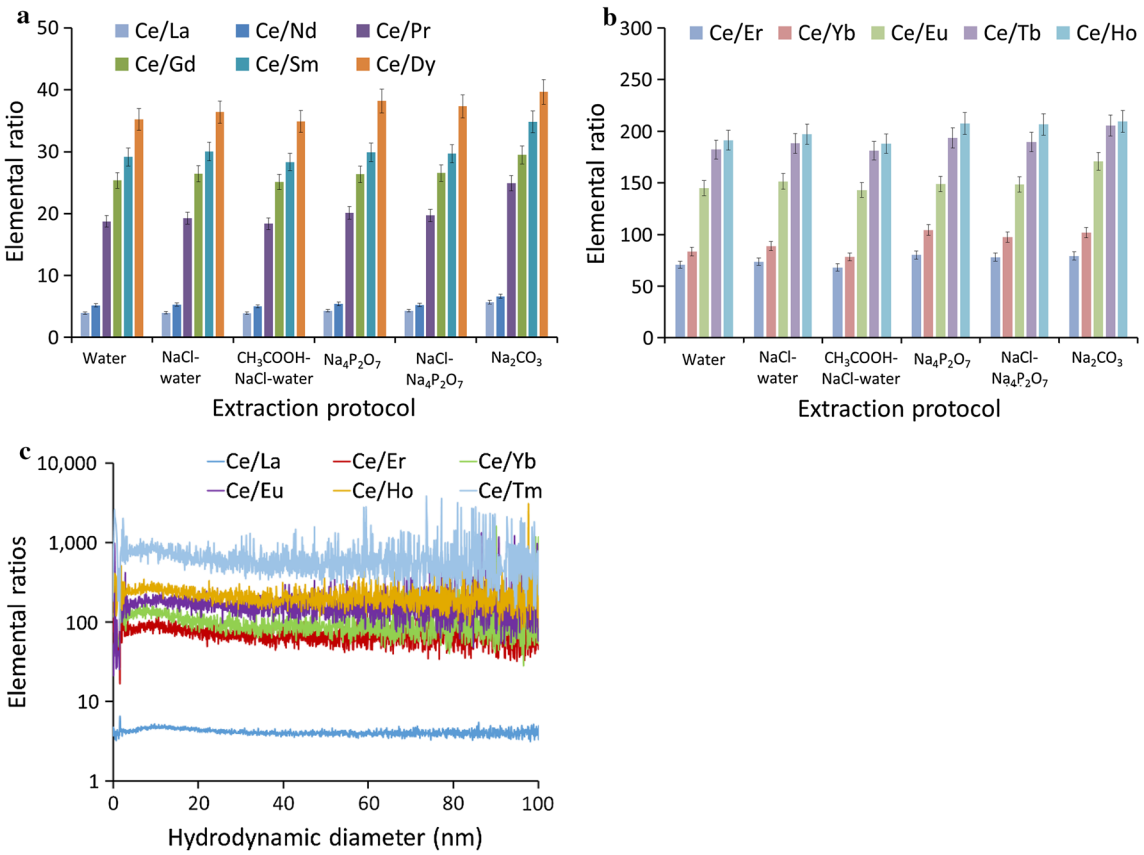

Fig. 3 Elemental ratios of Ce/rare earth elements based on **a**, **b** total metal digestion and **c** size-based elemental ratios obtained by asymmetric flow field-flow fractionation coupled with inductively coupled plasma-mass spectrometer for $Na_4P_2O_7$-extracted nanomaterials. The elemental ratios of Ce to rare earth elements are constant for natural nanomaterials extracted using different extractants, except for carbonate-extracted natural nanomaterials which show higher elemental ratios compared to the other extraction protocols. The elemental ratios of Ce to La, Er, Yb, Eu, Ho, and Tm are relatively constant ratios throughout the size range 20–100 nm, suggesting the co-occurrence of rare earth elements in natural nanomaterials. Injection volume was 100 µl

to the co-elution of Ce and rare earth elements at the same hydrodynamic diameters (representative examples are shown in Fig. S8a and b), suggesting the co-occurrence of rare earth elements in natural nanomaterials. Cerium is the most abundant rare earth element and is typically associated with other rare earth elements such as La, Er, Eu, Ho, Tm, and Yb in minerals such as monazite ((Ce,La,Th, Nd,Y)PO_4), xenotime ((Y,Ce)PO_4), allanite (Ca(Ce,La,Y,Ca)$Al_2(Fe^{2+},Fe^{3+})(SiO_4)(Si_2O_7)O(OH)$), and bastnasite ($(Ca(Ce, La)_2(CO_3)_3F_2$) (Murata et al. 1957; Long et al. 2012). The rare earth elements are commonly found together in Earth's crust because they share a trivalent charge and similar ionic radii. The high charge of the rare earth element ions impedes the ability of these elements to achieve charge balance and fit into the structure of the common rock-forming minerals, which have coordination sites best suited for valence states 2 or 1. As a result, for common silicate minerals such as amphiboles, feldspars, and olivine, most of the rare earth elements tend to remain in the coexisting melt. Successive generations of this process, referred to as crystal fractionation, increase the concentration of rare earth elements in the remaining melt until individual rare earth element-mineral-rich phases crystalize. In the coastal region of the south east of the USA, cerium occurs in natural minerals such as monazite (Zepf 2013; Ellefsen et al. 2015). The average size-based elemental ratios of Ce to La, Er, Yb, Eu, Ho, and Tm are in good agreement with those calculated based on total metal concentration (Table S4).

Ti/Nb, i.e., 320, Ti/Ta, i.e., 1846, and Ti/V, i.e., 10.4, show nearly constant ratios for all extraction protocols (Fig. 4a–c), suggesting strong association between Ti, Nb, Ta, and V. These elemental ratios are consistent with crustal values, suggesting the absence of anthropogenic TiO_2 engineered nanomaterials in this soil (Loosli et al. 2019). Size-based elemental ratios show a constant Ti/Nb and Ti/Ta ratios (Fig. 4d and e) due to the co-elution of Ti, Nb, and Ta at the same hydrodynamic diameters (Fig. S8c and d), suggesting the co-occurrence of Nb and Ta in natural nanomaterials. Size-based elemental distribution (Fig. 4f) shows that Ti, Fe, and V are correlated with a slight increase in Ti/V and slight decrease in Fe/V for larger sizes, ca. > 40 nm. TiO_2 in the southeastern USA coastal region commonly occurs as rutile, i.e., TiO_2, and ilmenite, i.e., $FeTiO_3$ (Ellefsen et al. 2015). Multi-element-single particle-inductively coupled plasma-mass analysis demonstrated the association between Ti, Al, Fe, Ce, Si, La, Ze, Nb, Ba, Th, Ta, W, and U in riverine TiO_2 natural nanomaterial on a particle-per-particle basis (Loosli et al. 2019). Nb and Ta are known to substitute Ti during mineral formation, and rutile and ilmenite are the most common host minerals for Ta and Nb (Kalfoun et al. 2002). Natural TiO_2 minerals, e.g., rutile and ilmenite, have been shown to be the dominant carrier, i.e., > 90–95% of the whole-rock content, for Ti, Nb, Ta, Sb, and W as well as an important carrier, i.e., 5–45% of the whole-rock content, for V, Cr, Mo, and Sn in TiO_2-bearing metamorphic rocks (Gaspar and Wyllie 1983; Nakashima and Imaoka 1998).

Previous studies suggested that the elemental ratios of Ti to rare earth elements can be used to differentiate TiO_2 natural nanomaterials from TiO_2-engineered nanomaterials (Gondikas et al. 2014). Thus, we evaluated the Ti/rare earth element ratios obtained by the different extraction protocols. Ti/rare earth element elemental ratios decreased for the $Na_4P_2O_7$- and Na_2CO_3-extracted natural nanomaterials (Fig. S9), suggesting that Ti and rare earth elements are either not associated or are partially associated. Figure S5a shows the co-elution of Ti and Ce in ultrapure water-extracted natural nanomaterials, whereas Figure S5e shows that Ti and Ce are eluted at different sizes in the $Na_4P_2O_7$-extracted natural nanomaterials. These findings suggest that Ti and Ce are associated together as different natural nanomaterials within small heteroaggregates and that ultrapure water extraction is insufficient to break these heteroaggregates. However, $Na_4P_2O_7$ and Na_2CO_3 can break these heteroaggregates into primary Ce- and Ti-rich natural nanomaterials with different hydrodynamic diameters. The decrease in Ti/rare earth elements ratio in $Na_4P_2O_7$- and Na_2CO_3-extracted natural nanomaterials relative to ultrapure water- and NaCl-extracted natural nanomaterials can be attributed to the selective extraction of rare earth elements by $Na_4P_2O_7$ and Na_2CO_3.

Conclusion

Understanding the properties of natural nanomaterials such as size, size distribution, morphology, elemental composition, and elemental ratios is essential to better understand natural nanomaterials and/or their environmental behaviors and functions, but also to develop approaches to detect and quantify engineered nanomaterials in soils. For the soil investigated in this study, $Na_4P_2O_7$ dispersed the highest concentration of natural nanomaterials with the smallest size distribution. Ultrapure water, NaCl–ultrapure water and CH_3COOH–NaCl–ultrapure water together with sonication dispersed only a small fraction of natural nanomaterials in the form of aggregates of primary natural nanomaterials. This study also evaluated the elemental association and ratios within natural nanomaterials, and demonstrated that Ce is strongly associated with rare earth elements and that Ti is strongly associated with Nb, Ta, and V. Therefore, these elemental associations and ratios can potentially be used as signatures to trace CeO_2- and TiO_2-engineered nanomaterials in the environment. Future studies will investigate the effect of extractants on natural nanomaterial extraction efficiency from different soils and determine the elemental ratios, e.g., Ti to Nb, Ta, and V, and Ce to La, in natural nanomaterials from different soils.

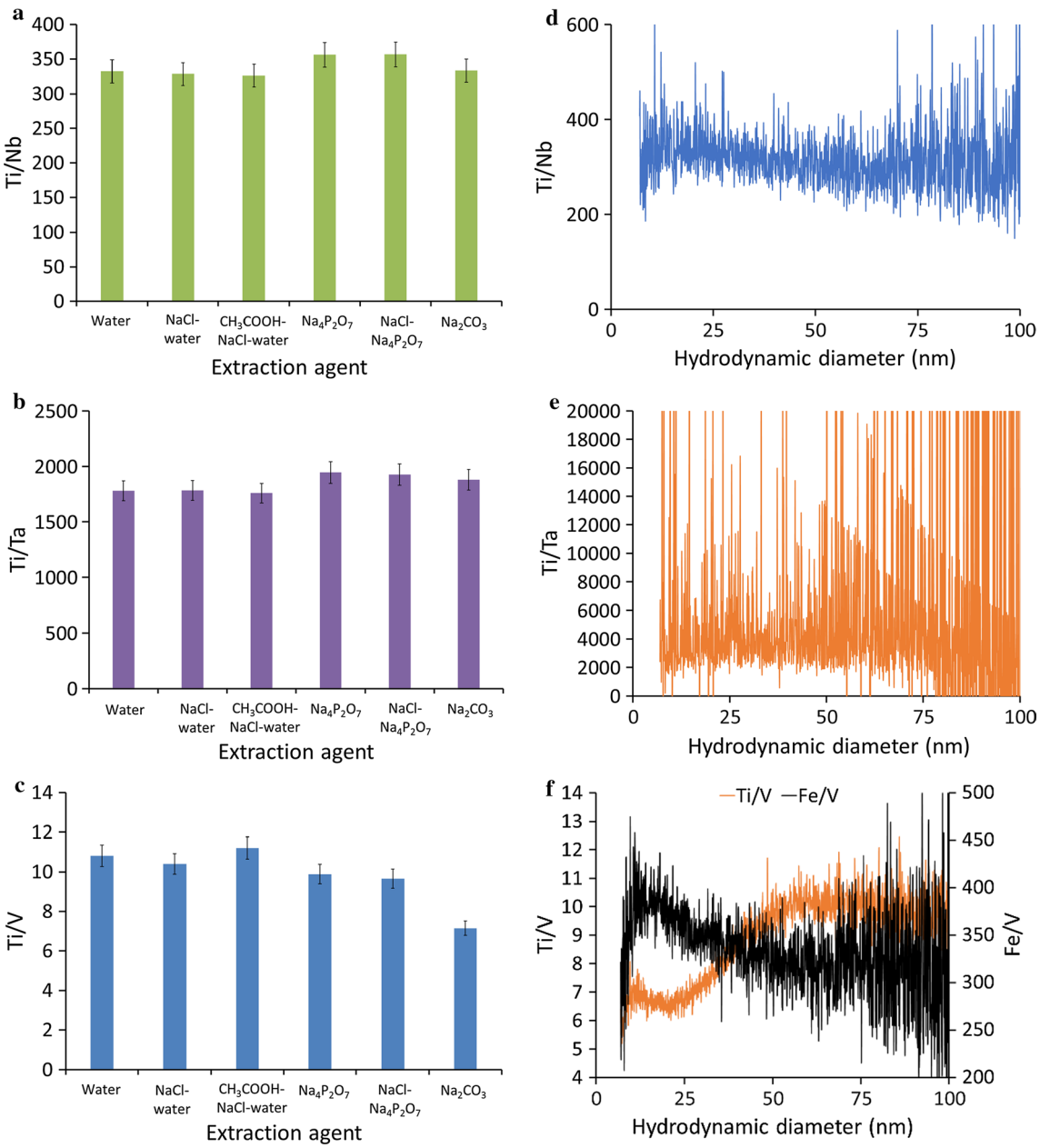

Fig. 4 **a**–**c** Elemental ratios based on total metal concentrations as a function of extraction protocols. Size-based elemental ratios obtained by asymmetric flow-field-flow fractionation coupled with inductively coupled plasma-mass spectrometer for $Na_4P_2O_7$-extracted natural nanomaterials of **d** Ti/Nb, **e** Ti/Ta, and **f** Ti/V and Fe/V. Ti/Nb, Ti/Ta, and Ti/V show nearly constant ratios for all extractants, suggesting strong association between Ti, Nb, Ta, and V. Injection volume was 100 µl

Acknowledgements We acknowledge funding from the US National Science Foundation (NSF#1553909), China Scholarship Council (CSC_201606380069) and the Swiss National Foundation (P2GEP2_165046). This work was supported by the Virginia Tech National Center for Earth and Environmental Nanotechnology Infrastructure (NanoEarth), a member of the National Nanotechnology Coordinated Infrastructure (NNCI), supported by NSF (ECCS 1542100).

References

Abbaspour A, Baramakeh L (2006) Application of principle component analysis–artificial neural network for simultaneous determination of zirconium and hafnium in real samples. Spectrochim Acta A Mol Biomol Spectrosc 64:477–482. https://doi.org/10.1016/j.saa.2005.07.047

Alvarez PJJ, Colvin V, Lead J, Stone V (2009) Research priorities to advance eco-responsible nanotechnology. ACS Nano 3:1616–1619. https://doi.org/10.1021/nn9006835

Baalousha M (2009) Aggregation and disaggregation of iron oxide nanoparticles: Influence of particle concentration, pH and natural organic matter. Sci Total Environ 407:2093–2101. https://doi.org/10.1016/j.scitotenv.2008.11.022

Baalousha M, Kammer FVD, Motelica-Heino M, Coustumer PL (2005) 3D characterization of natural colloids by FlFFF-MALLS-TEM. Anal Bioanal Chem 383:549–556. https://doi.org/10.1007/s00216-005-0006-9

Baalousha M, Kammer FVD, Motelica-Heino M et al (2006) Size fractionation and characterization of natural colloids by flow-field flow fractionation coupled to multi-angle laser light scattering. J Chromatogr A 1104:272–281. https://doi.org/10.1016/j.chroma.2005.11.095

Baalousha M, Ju-Nam Y, Cole PA et al (2012) Characterization of cerium oxide nanoparticles—part 2: nonsize measurements. Environ Toxicol Chem 31:994–1003. https://doi.org/10.1002/etc.1786

Baalousha M, Prasad A, Lead JR (2014) Quantitative measurement of the nanoparticle size and number concentration from liquid suspensions by atomic force microscopy. Environ Sci Process Impacts 16:1338–1347. https://doi.org/10.1039/c3em00712j

Buffle J, Wilkinson KJ, Stoll S et al (1998) A generalized description of aquatic colloidal interactions: the three-colloidal component approach. Environ Sci Technol 32:2887–2899. https://doi.org/10.1021/es980217h

Calabi-Floody M, Bendall JS, Jara AA et al (2011) Nanoclays from an Andisol: extraction, properties and carbon stabilization. Geoderma 161:159–167. https://doi.org/10.1016/j.geoderma.2010.12.013

Chen KL, Mylon SE, Elimelech M (2006) Aggregation kinetics of alginate-coated hematite nanoparticles in monovalent and divalent electrolytes. Environ Sci Technol 40:1516–1523. https://doi.org/10.1021/es0518068

Dev A, Srivastava AK, Karmakar S (2018) Nanomaterial toxicity for plants. Environ Chem Lett 16:85–100. https://doi.org/10.1007/s10311-017-0667-6

Ellefsen KJ, Van Gosen BS, Fey DL et al (2015) First steps of integrated spatial modeling of titanium, zirconium, and rare earth element resources within the Coastal Plain sediments of the southeastern United States. U.S. Geological Survey, Reston, VA

Fedotov PS, Vanifatova NG, Shkinev VM, Spivakov BY (2011) Fractionation and characterization of nano-and microparticles in liquid media. Anal Bioanal Chem 400:1787–1804. https://doi.org/10.1007/s00216-011-4704-1

Frisby C, Bizimis M, Mallick S (2016) Hf–Nd isotope decoupling in bulk abyssal peridotites due to serpentinization. Chem Geol 440:60–72. https://doi.org/10.1016/j.chemgeo.2016.07.006

Gaspar JC, Wyllie PJ (1983) Ilmenite (high Mg, Mn, Nb) in the carbonatites from the Jacupiranga Complex, Brazil. Am Mineral 68:960–971

Gondikas AP, von der Kammer F, Reed RB et al (2014) Release of TiO_2 nanoparticles from sunscreens into surface waters: a one-year survey at the old Danube recreational Lake. Environ Sci Technol 48:5415–5422. https://doi.org/10.1021/es405596y

Gondikas A, von der Kammer F, Kaegi R et al (2018) Where is the nano? Analytical approaches for the detection and quantification of TiO_2 engineered nanoparticles in surface waters. Environ Sci Nano 5:313–326. https://doi.org/10.1039/c7en00952f

IARC (International Agency for Research on Cancer) (2010) Carbon black, titanium dioxide, and talc. IARC Press, International Agency for Research on Cancer, Lyon

Illés E, Tombácz E (2006) The effect of humic acid adsorption on pH-dependent surface charging and aggregation of magnetite nanoparticles. J Colloid Interface Sci 295:115–123. https://doi.org/10.1016/j.jcis.2005.08.003

Jones JV III, Piatak NM, Bedinger GM (2017) Zirconium and hafnium. U.S. Geological Survey, Reston, VA

Kahlon SK, Sharma G, Julka JM et al (2018) Impact of heavy metals and nanoparticles on aquatic biota. Environ Chem Lett 16:919–946. https://doi.org/10.1007/s10311-018-0737-4

Kalfoun F, Ionov D, Merlet C (2002) HFSE residence and Nb/Ta ratios in metasomatised, rutile-bearing mantle peridotites. Earth Planet Sci Lett 199:49–65. https://doi.org/10.1016/S0012-821X(02)00555-1

Koopmans GF, Groenenberg JE (2011) Effects of soil oven-drying on concentrations and speciation of trace metals and dissolved organic matter in soil solution extracts of sandy soils. Geoderma 161:147–158. https://doi.org/10.1016/j.geoderma.2010.12.012

Kretzschmar R, Sticher H (1997) Transport of humic-coated iron oxide colloids in a sandy soil: influence of Ca^{2+} and trace metals. Environ Sci Technol 31:3497–3504. https://doi.org/10.1021/es970244s

Lead JR, Batley GE, Alvarez PJJ et al (2018) Nanomaterials in the environment: behavior, fate, bioavailability, and effects—an updated review. Environ Toxicol Chem 37:2029–2063. https://doi.org/10.1002/etc.4147

Li W, He Y, Wu J, Xu J (2012) Extraction and characterization of natural soil nanoparticles from Chinese soils. Eur J Soil Sci 63:754–761. https://doi.org/10.1111/j.1365-2389.2012.01480.x

Long KR, Van Gosen BS, Foley NK, Cordier D (2012) The principal rare earth elements deposits of the United States: a summary of domestic deposits and a global perspective. In: Sinding-Larsen R, Wellmer FW (eds) Non-renewable resource issues. Springer, Dordrecht, pp 131–155. https://doi.org/10.1007/978-90-481-8679-2_7

Loosli F, Yi Z, Berti D, Baalousha M (2018) Toward a better extraction of titanium dioxide engineered nanomaterials from complex environmental matrices. NanoImpact 11:119–127. https://doi.org/10.1016/j.impact.2018.06.002

Loosli F, Wang J, Rothenberg S et al (2019) Sewage spills are a major source of titanium dioxide engineered (nano)-particle release into the environment. Environ Sci Nano 6:763–777. https://doi.org/10.1039/c8en01376d

Luo J, Ying K, Bai J (2005) Savitzky–Golay smoothing and differentiation filter for even number data. Signal Process 85:1429–1434. https://doi.org/10.1016/j.sigpro.2005.02.002

Meisterjahn B, Neubauer E, Von der Kammer F et al (2014) Asymmetrical flow-field-flow fractionation coupled with inductively coupled plasma mass spectrometry for the analysis of gold nanoparticles in the presence of natural nanoparticles. J Chromatogr A 1372:204–211. https://doi.org/10.1016/j.chroma.2014.10.093

Montaño MD, Lowry GV, von der Kammer F et al (2014) Current status and future direction for examining engineered nanoparticles in natural systems. Environ Chem 11:351–366. https://doi.org/10.1071/en14037

Morel MLA, Nebel O, Nebel-Jacobsen YJ et al (2008) Hafnium isotope characterization of the GJ-1 zircon reference material by solution and laser-ablation MC-ICPMS. Chem Geol 255:231–235. https://doi.org/10.1016/j.chemgeo.2008.06.040

Murata KJ, Rose HJ Jr, Carron MK, Glass JJ (1957) Systematic variation of rare-earth elements in cerium-earth minerals. Geochim Cosmochim Acta 11:141–161. https://doi.org/10.1016/0016-7037(57)90077-7

Nakashima K, Imaoka T (1998) Niobian and zincian ilmenites in syenites from Cape Ashizuri, Southwest Japan. Mineral Petrol 63:1–17. https://doi.org/10.1007/bf01162765

Navratilova J, Praetorius A, Gondikas A et al (2015) Detection of engineered copper nanoparticles in soil using single particle ICP-MS. Int J Environ Res Public Health 12:15756–15768. https://doi.org/10.3390/ijerph121215020

NCSS (National Cooperative Soil Survey) (2019) Primary characterization data of Lucy series. https://ncsslabdatamart.sc.egov.usda.gov/rptExecute.aspx?p=73066&r=1&. Accessed 24 July 2019

Pansu M, Gautheyrou J (2007) Handbook of soil analysis: mineralogical, organic and inorganic methods. Springer, Berlin

Patchett PJ, Kouvo O, Hedge CE, Tatsumoto M (1982) Evolution of continental crust and mantle heterogeneity: evidence from Hf isotopes. Contrib Mineral Petrol 78:279–297. https://doi.org/10.1007/BF00398923

Philippe A, Campos D, Guigner J-M et al (2018) Characterization of the natural colloidal TiO_2 background in soil. Separations 5:50. https://doi.org/10.3390/separations5040050

Piccinno F, Gottschalk F, Seeger S, Nowack B (2012) Industrial production quantities and uses of ten engineered nanomaterials in Europe and the world. J Nanopart Res 14:1109. https://doi.org/10.1007/s11051-012-1109-9

Plathe KL, Von der Kammer F, Hassellöv M et al (2010) Using FlFFF and aTEM to determine trace metal–nanoparticle associations in riverbed sediment. Environ Chem 7:82–93. https://doi.org/10.1071/EN09111

Praetorius A, Gundlach-Graham A, Goldberg E et al (2017) Single-particle multi-element fingerprinting (spMEF) using inductively-coupled plasma time-of-flight mass spectrometry (ICP-TOFMS) to identify engineered nanoparticles against the elevated natural background in soils. Environ Sci Nano 4:307–314. https://doi.org/10.1039/c6en00455e

Prasad A, Lead JR, Baalousha M (2015) An electron microscopy based method for the detection and quantification of nanomaterial number concentration in environmentally relevant media. Sci Total Environ 537:479–486. https://doi.org/10.1016/j.scitotenv.2015.07.117

Pronk JT, Johnson DB (1992) Oxidation and reduction of iron by acidophilic bacteria. Geomicrobiol J 10:153–171. https://doi.org/10.1080/01490459209377918

Regelink IC, Weng L, Koopmans GF, van Riemsdijk WH (2013) Asymmetric flow field-flow fractionation as a new approach to analyse iron-(hydr)oxide nanoparticles in soil extracts. Geoderma 202–203:134–141. https://doi.org/10.1016/j.geoderma.2013.03.015

Rottman J, Sierra-Alvarez R, Shadman F (2013) Real-time monitoring of nanoparticle retention in porous media. Environ Chem Lett 11:71–76. https://doi.org/10.1007/s10311-012-0381-3

Sardoiwala MN, Kaundal B, Choudhury SR (2018) Toxic impact of nanomaterials on microbes, plants and animals. Environ Chem Lett 16:147–160. https://doi.org/10.1007/s10311-017-0672-9

Siripinyanond A, Barnes RM, Amarasiriwardena D (2002) Flow field-flow fractionation-inductively coupled plasma mass spectrometry for sediment bound trace metal characterization. J Anal At Spectrom 17:1055–1064. https://doi.org/10.1039/b202734h

Tang ZY, Wu LH, Luo YM, Christie P (2009) Size fractionation and characterization of nanocolloidal particles in soils. Environ Geochem Health 31:1–10. https://doi.org/10.1007/s10653-008-9131-7

Tatzber M, Stemmer M, Spiegel H et al (2007) FTIR-spectroscopic characterization of humic acids and humin fractions obtained by advanced NaOH, $Na_4P_2O_7$, and Na_2CO_3 extraction procedures. J Plant Nutr Soil Sci 170:522–529. https://doi.org/10.1002/jpln.200622082

Taylor SR, McLennan SM (1985) The continental crust: its composition and evolution. Blackwell Scientific Publications, Hoboken

Theng BKG, Yuan GD (2008) Nanoparticles in the soil environment. Elements 4:395–399. https://doi.org/10.2113/gselements.4.6.395

Tunç S, Duman O, Kancı B (2012) Rheological measurements of Na-bentonite and sepiolite particles in the presence of tetradecyltrimethylammonium bromide, sodium tetradecyl sulfonate and Brij 30 surfactants. Colloids Surf Physicochem Eng Asp 398:37–47. https://doi.org/10.1016/j.colsurfa.2012.02.006

van Zomeren A, Comans RN (2007) Measurement of humic and fulvic acid concentrations and dissolution properties by a rapid batch procedure. Environ Sci Technol 41:6755–6761. https://doi.org/10.1021/es0709223

Verrall KE, Warwick P, Fairhurst AJ (1999) Application of the Schulze–Hardy rule to haematite and haematite/humate colloid stability. Colloids Surf Physicochem Eng Asp 150:261–273. https://doi.org/10.1016/S0927-7757(98)00858-9

von der Kammer F, Ferguson PL, Holden PA et al (2012) Analysis of engineered nanomaterials in complex matrices (environment and biota): General considerations and conceptual case studies. Environ Toxicol Chem 31:32–49. https://doi.org/10.1002/etc.723

Wedepohl KH (1969) Handbook of geochemistry. Springer, Berlin

Zepf V (2013) Rare earth elements: what and where they are. In: Zepf V (ed) Rare earth elements: a new approach to the nexus of supply, demand and use: exemplified along the use of neodymium in permanent magnets. Springer, Berlin, pp 11–39